

TURBULENCE IN PRECESSING CONTAINERS

Susumu Goto, Ken Komoda, and Jun Kanki

Graduate School of Engineering Science, Osaka University
 1-3 Machikaneyama, Toyonaka, Osaka, 560-8531 Japan
 goto@me.es.osaka-u.ac.jp

ABSTRACT

By means of direct numerical simulations, we investigate turbulence of an incompressible fluid confined in precessing containers. In the numerical scheme by a finite-difference method (Komoda & Goto, 2019), we use a flexible grid generation algorithm so that we can simulate turbulence in a precessing sphere, spheroids, and cylinders. We reveal the transition route to developed turbulence and its sustaining mechanism in these containers. When we fix the spin rate and increase the precession rate from zero, the internal flow in each container changes to be the solid-body rotational flow about the spin axis, periodic flow, weak turbulence without small-scale turbulent eddies, and developed turbulence. The most developed turbulence is sustained when the magnitude of the precession angular velocity is about 10 % of the spin in the case that precession axis is perpendicular to the spin axis. Stronger precession drastically reduces the turbulence in a central region of the containers and leads to two-dimensionalization along the precession axis. The transition from steady flow to developed turbulence is continuous for the precessing sphere, whereas it is accompanied by a hysteresis loop for spheroids (with a sufficiently large ellipticity η) and cylinders. We also show that the most developed turbulence in these containers always has a pair of twisted three-dimensional container-size vortices. The large-scale shear flow around these vortices stretch and amplify small-scale turbulent eddies.

INTRODUCTION

The target of the present study is turbulence driven by the precession of a container. Here, the ‘‘precession’’ is defined by the rotation of the spin axis of a rotating object (Fig. 1). In the followings, the angular velocities of the spin and precession are denoted by $\boldsymbol{\Omega}_s$ and $\boldsymbol{\Omega}_p$, respectively. In the present study, we consider only the case that $\boldsymbol{\Omega}_s \perp \boldsymbol{\Omega}_p$.

Turbulence in a precessing container (sphere, spheroid, and cylinder) has been extensively studied by many researchers, in particular, by geophysicists because the Earth is precessing slowly (in a period of about 26 000 years) and because the generation mechanism of geodynamo is a central issue of the field. This flow system is attractive also in engineering applications. Furthermore, the physics behind the sustainability of the strong turbulence is a scientifically important unsolved problem. We emphasize that this flow system is one of the canonical wall-bounded flows, which has been studied since the age of Poincaré (1910).

Modern studies of this flow system were triggered by the laboratory experiments by Malkus (1968) and the theory by Busse (1968). The former experiments showed that

developed turbulence was sustained in a weakly precessing ($\Omega_p < \Omega_s$) sphere and spheroid. On the other hand, the latter theory analytically derives steady flows in precessing spheroids. Fifty years have passed since these seminal studies, and many experimental and theoretical studies were conducted. However, the detailed route to developed turbulence and its sustaining mechanism have not yet been revealed. This is because it is hard to experimentally investigate three-dimensional flow structures, and because theoretical studies are limited within the linear regime. In the present study, we conduct a series of the direct numerical simulations (DNS) of *developed turbulence* in a precessing sphere, spheroids, and cylinders with systematically changing control parameters. The main aim of our DNS is to reveal the transitional route to developed turbulence, the three-dimensional structures of the turbulence, their sustaining mechanism, and its dependence on the container’s shape.

CONTROL PARAMETERS

We non-dimensionalize the governing equations by using the size a (the equatorial radius of the sphere and spheroid or the radius of the cross-section of the cylinder) as a characteristic length-scale and the reciprocal Ω_s^{-1} of the spin angular velocity as a characteristic time-scale of the system. Then, the non-dimensional velocity $\mathbf{u}(\mathbf{x}, t)$ and pressure $p(\mathbf{x}, t)$ of the confined incompressible fluid (the kinematic viscosity of which is denoted by ν) are governed by

$$\nabla \cdot \mathbf{u} = 0 \quad (1)$$

and

$$\frac{\partial \mathbf{u}}{\partial t} + \mathbf{u} \cdot \nabla \mathbf{u} = -\nabla p + \frac{1}{Re} \nabla^2 \mathbf{u} + 2Po \mathbf{u} \times \hat{\mathbf{e}}_p. \quad (2)$$

Equation (2) is described in the frame rotating at the constant angular velocity $\boldsymbol{\Omega}_p (= \Omega_p \hat{\mathbf{e}}_p)$ with respect to the laboratory. Thus, the third term on the right-hand side is the Coriolis force, and p includes the centrifugal potential. Note that (2) depends on two non-dimensional parameters:

$$Re = \frac{a^2 \Omega_s}{\nu} \quad (\text{Reynolds number}) \quad (3)$$

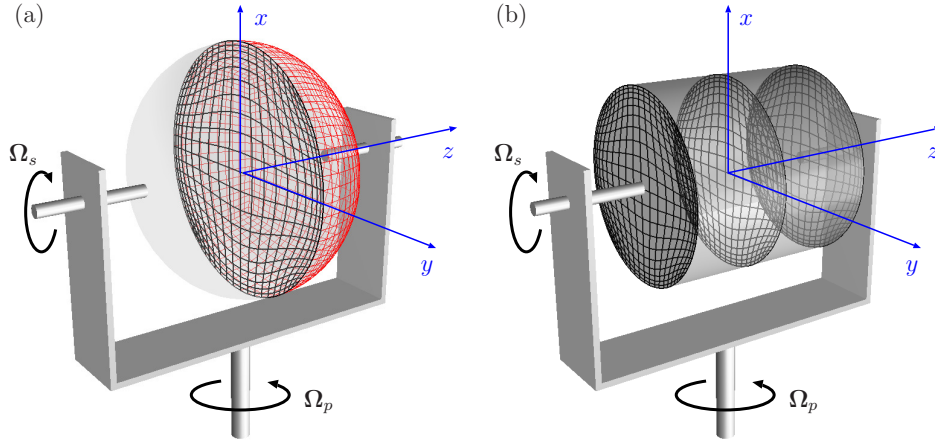


Figure 1. (a) Precessing spheroid. The numerical grid is drawn on the surface of the hemi-spheroid ($z > 0$) and on the equatorial plane ($z = 0$). Note that the grid is boundary-fitted and does not have a coordinate singularity. For visibility, we reduced the number of grid points. (b) Precessing cylinder. The numerical grid (with a reduced number of grid points) is drawn on the equatorial planes and bottoms of the cylinder.

and

$$Po = \frac{\Omega_p}{\Omega_s} \quad (\text{Poincaré number}). \quad (4)$$

These parameters indicate the spin and precession rates, respectively. We impose the non-slip boundary condition on the container's wall. Therefore, once we fix the shape of the container, in addition to these two parameters (Re, Po) , a shape parameter such as the ellipticity $\eta = (a - b)/a$ for a spheroid with the polar radius b [Fig. 1(a)] or the aspect ratio $\Gamma = L/(2a)$ for a cylinder with the axial length L [Fig. 1(b)] controls the flow state. Hence, the control parameters are (Re, Po, η) for spheroids and (Re, Po, Γ) for cylinders.

DIRECT NUMERICAL SIMULATIONS

We solve the governing equations (1) and (2) by a finite-difference method. We use the second-order central difference for the spatial derivatives, and the second-order Crank-Nicolson method for the viscous term and the second-order Adams-Bashforth method for the other terms in (2) for the temporal integration.

Although these numerical schemes are standard, our ingenious method is in the construction of the numerical grid. We do not use the spherical or cylindrical coordinates which are usually used in the DNS of flow in a sphere, spheroids, and cylinders. Instead, we use a boundary-fitted grid shown in Fig. 1. The numerical grid for a spheroid [Fig. 1(a)] is constructed by solving the Poisson equation, the boundary condition of which is the so-called cubed sphere grid. Thus obtained grid does not have a coordinate singularity in the domain (for example, at the center of the sphere), and, more importantly, we can concentrate the grid points near the wall, where fine-scale flow structures appear. Details of the grid generation algorithm are given in Komoda & Goto (2019). We also emphasize that we can easily, without modifying the main DNS code, change the shape of the container. Thanks to this advantage, we conduct the DNS of flow in spheroids [Fig. 1(a)] and cylinders [Fig. 1(b)].

We have conducted grid refinement studies and verified that the DNS results, with 98^3 grid points, are in good agreement with the experimental data under the same condition (Re, Po, η) (see Fig. 2 in Komoda & Goto, 2019). This implies that, although the grid used in the present DNS has strongly distorted cells near the boundary, the numerical accuracy is sufficient for the present purpose.

TRANSITION TO TURBULENCE

For all the containers examined by the present DNS, for a fixed Re (the spin rate), when increasing Po (the precession rate), the flow state changes as the solid-body rotation about the spin axis ($Po = 0$), steady flow ($Po \ll 1$), periodic flow, weak turbulence, and developed turbulence ($Po = O(0.1)$). The steady flow is well described by Busse (1968)'s solution, and the instabilities of the steady flow were also investigated (Kerswell, 1993; Lin *et al.*, 2015). However, the fully non-linear regime where strong turbulence is sustained has not been well investigated. The most developed turbulence is sustained with a relatively weak precession ($Po \approx 0.1$), and if we further increase Po (say, $Po \gtrsim 0.3$) turbulence in the container is drastically reduced along the precession axis (\hat{e}_p), which is a well-known phenomenon in rotating systems. These numerical results are consistent with our previous experimental results (Goto *et al.*, 2007, 2014; Horimoto *et al.*, 2018) for the precessing sphere and spheroids.

The transition route to the developed turbulence (as increasing Po) in precessing spheroids are shown in Fig. 2(a). This figure shows the spatio-temporal average K of the kinetic energy in the precessing spheroid as a function of Po for fixed $Re (= 10^4)$. The ellipticity is set as $\eta = 0, 0.1, 0.15$, and 0.2 . Note that K is estimated in the frame rotating at Ω_p and that K attains its maximum for $Po = 0$ and it decreases with Po . $K \rightarrow 0$ as $Po \rightarrow \infty$ because the flow tends to the solid-body rotation about the precession axis in this limit. When K is large, the flow is approximated as a uniform-vorticity flow [Fig. 2(b)]. The large- K states do not accompany small-scale turbulent eddies. In contrast, the developed turbulence with small-scale disordered eddies is sustained when K is small ($K \approx 0.2$) as shown in Fig. 2(c)

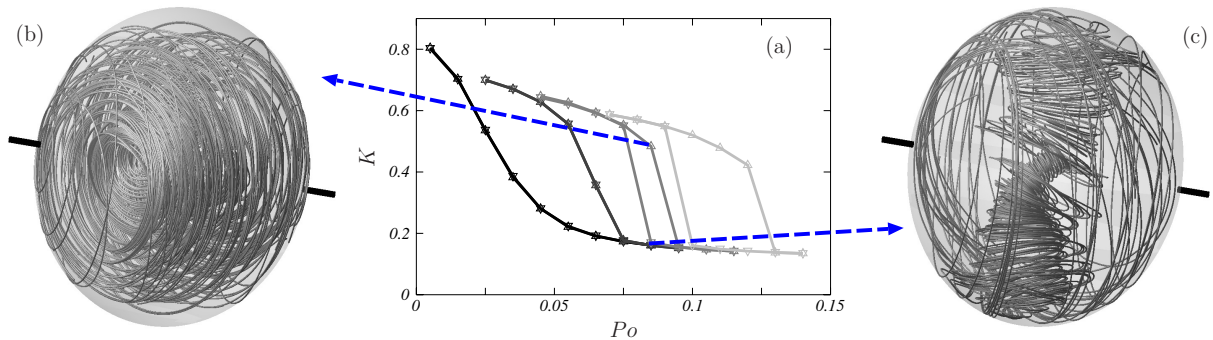


Figure 2. (a) Transition to developed turbulence for a fixed spin rate $Re = 10^4$ and changing the precession rate Po in the spheroids with the ellipticity $\eta = 0$ (black), 0.1 (dark gray), 0.15 (gray), and 0.2 (light gray). The upper-triangles denote the results with increasing Po , while lower-triangles denote those with decreasing Po . The transition is discontinuous for larger ellipticity ($\eta > 0.1$) and hysteresis loops are observed. (b, c) There exist bistable states at $(Re, Po, \eta) = (10^4, 0.085, 0.15)$. Gray curves are streamlines of the mean flow. As shown in Fig. 3 small-scale turbulent eddies are crated around this large-scale structure shown in (c).

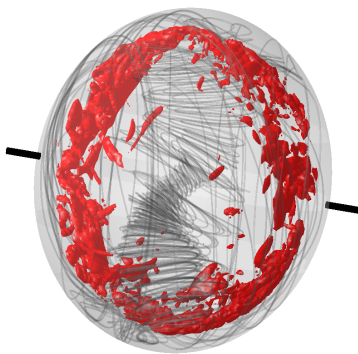


Figure 3. Small-scale turbulent eddies in precessing spheroid ($\eta = 0.1$). Red blobs are the isosurfaces of the instantaneous enstrophy for the same flow condition as in Fig. 2(c). Turbulent vortices are created around the large-scale vortex visualized by mean-flow streamlines (gray curves).

and Fig. 3.

Figure 2(a) shows that the developed turbulence appears through a continuous transition for the sphere ($\eta = 0$) and the spheroid with $\eta = 0.1$, whereas the transition is accompanied by a hysteresis loop for spheroids with ellipticity larger than 0.1 for this Re . For example, for a given set of parameters $(Re, Po, \eta) = (10^4, 0.085, 0.15)$, we can observe bistable states. One is weak turbulence [Fig. 2(b)], and the other is developed turbulence [Fig. 2(c) and Fig. 3]. The present DNS realize these phenomena previously observed in laboratory experiments (Malkus, 1968; Horimoto *et al.*, 2018).

It is interesting to show that this qualitative difference of the transition (for the sphere and spheroids) to turbulence is well described by using the *steady* solution by Busse (1968). For example, we show, by using the solution, that the discontinuous (i.e. subcritical) transition occurs when $\eta > 10/Re^{1/2}$ (Komoda & Goto, 2019). This expression well explains the DNS results [Fig. 2(a)] as well as our experimental observation (Horimoto *et al.*, 2018). Similar analyses of the transition on the basis of Busse's steady solution were also made by other authors (Lorenzani

& Tilgner, 2003; Noir *et al.*, 2003).

Furthermore, the present DNS shows that the developed turbulence appears through a subcritical transition also in the precessing cylinder with the aspect ratio $\Gamma = 1$. This DNS result is consistent with experiments by Herault *et al.* (2015). The DNS for different values of Γ are in progress and will be reported elsewhere in the near future.

SUSTAINING MECHANISM OF TURBULENCE

As mentioned in the introduction, the most remarkable feature of this flow system is that the simple motion of the container drives non-trivial complex flow. In this section, we summarize our knowledge, which was revealed by the present DNS, about the three-dimensional turbulent flow structures and their sustaining mechanism.

The key to the understanding of the sustaining mechanism is large-scale coherent flow vortical structures in the containers. In all the precessing containers examined, we observe twisted vortical structures (Fig. 4) when the developed turbulence is sustained. These structures are identified by the streamlines of the mean flow. It is the shear flow around these twisted vortices that create small-scale turbulent eddies. The direct evidence of this mechanism is shown in Fig. 3. We observe that turbulent vortices (red isosurfaces) are created in the region with high strain rates. This mechanism of small-scale turbulent vortices is consistent with the experimental results for the precessing sphere (Horimoto & Goto, 2017). The present DNS show that not only in the sphere but also in the precessing spheroids with a finite ellipticity or even a cylinder, small-scale turbulence is sustained by being stretched and amplified in the shear flow around the twisted large-scale vortices (Fig. 4).

The final step to describe the sustaining mechanism of the precession-driven turbulence is to explain the origin of the non-trivial large-scale (cavity-size) twisted vortices (Fig. 4). To show the origin, we investigate the Po -dependence of them for a fixed Re and η (or Γ). Then, the observed flow structures in Fig. 4 are explained as a simple structure, which appears for small Po , deformed due to the Coriolis force.

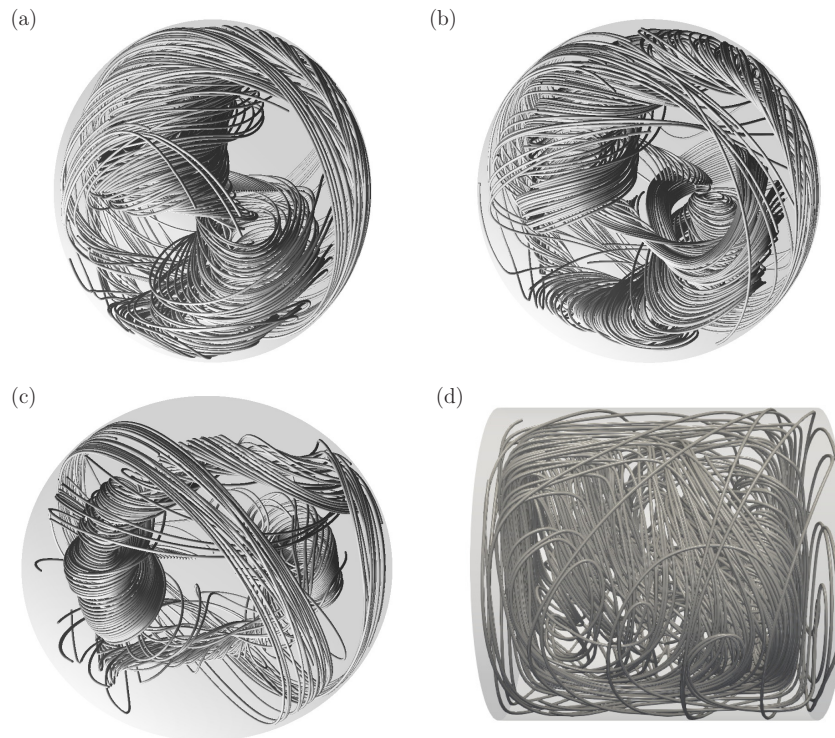


Figure 4. Streamlines of the temporally-averaged velocity in the precessing (a) oblate spheroid ($\eta = 0.1$), (b) sphere ($\eta = 0$), (c) prolate spheroids ($\eta = -0.1$), and (d) cylinder ($\Gamma = 1$). $Re = 10^4$. $Po = 0.1$. In all the cases, the large-scale flow is composed of a pair of twisted vortices.

CONCLUSION

The flow in a precessing container (Fig. 1) is a canonical wall-bounded flow. By conducting DNS, we have revealed (i) the transitional route to developed turbulence, (ii) three-dimensional flow structures in the developed turbulence, and (iii) their sustaining mechanism in precessing containers. Our DNS employ the numerical grid shown in Fig. 1. It is advantageous in the DNS that we can easily change the shape of the containers, and we have conducted the DNS of developed turbulence sustained in a precessing sphere, spheroids, and cylinders. The present NS show that the transition to the developed turbulence is continuous in the sphere, while it is accompanied by a hysteresis loop for the spheroids with a non-negligible ellipticity $\eta > 10/Re^{1/2}$ [Fig. 2(a)] and in cylinders. The most important conclusion of the present study is that a pair of twisted large-scale vortices always exists in the developed turbulence (sustained for $Po \approx 0.1$ in these containers; see Fig. 4) and shear flow around these vortices stretches and amplifies the small-scale turbulent eddies (Fig. 3).

This study was partly supported by JSPS Grant-in-Aid for Scientific Research (16H04268). Some of the DNS were conducted under the auspices of the NIFS Collaboration Research Programs (NIFS17KNSS101, NIFS18KNSS108).

REFERENCES

Busse, F. H. 1968 Steady fluid flow in a precessing spheroidal shell. *J. Fluid Mech.* **33**, 739–751.
 Goto, S., Ishii, N., Kida, S. & Nishioka, M. 2007 Turbulence generator using a precessing sphere. *Phys. Fluids* **19**, 061705.

Goto, S., Matsunaga, A., Fujiwara, M., Nishioka, M., Kida, S., Yamato, M. & Tsuda, S. 2014 Turbulence driven by precession in spherical and slightly elongated spheroidal cavities. *Phys. Fluids* **26**, 055107.
 Herault, J., Gundrum, T., Giesecke, A. & Stefani, F. 2015 Subcritical transition to turbulence of a precessing flow in a cylindrical vessel. *Phys. Fluids* **27**, 124102.
 Horimoto, Y. & Goto, S. 2017 Sustaining mechanism of small-scale turbulent eddies in a precessing sphere. *Phys. Rev. Fluids* **2**, 114603.
 Horimoto, Y., Simonet-Davin, G., Katayama, A. & Goto, S. 2018 Impact of a small ellipticity on the sustainability condition of developed turbulence in a precessing spheroid. *Phys. Rev. Fluids* **3**, 044603.
 Kerswell, R. R. 1993 The instability of precession flow. *Geophys. Astrophys. Fluid Dyn.* **72**, 107–144.
 Komoda, K. & Goto, S. 2019 Three-dimensional flow structures of turbulence in precessing spheroids. *Phys. Rev. Fluids* **4**, 014603.
 Lin, Y., Marti, P. & Noir, J. 2015 Shear-driven parametric instability in a precessing sphere. *Phys. Fluids* **27**, 046601.
 Lorenzani, S. & Tilgner, A. 2003 Inertial instabilities of fluid flow in precessing spheroidal shells. *J. Fluid Mech.* **492**, 363–379.
 Malkus, W. V. R. 1968 Precession of the earth as the cause of geomagnetism. *Science* **160**, 259–264.
 Noir, J., Cardin, P., Jault, D. & Masson, J.-P. 2003 Experimental evidence of nonlinear resonance effects between retrograde precession and the tilt-over mode within a spheroid. *Geophys. J. Int.* **154**, 407–416.
 Poincaré, H. 1910 Sur la précession des corps déformables. *Bull. Astron.* **27**, 321–356.